



# Evaluating Urban Geometry Impacts on Incident Solar Radiation on Building Envelopes

Zhifeng Wu<sup>1</sup> · Yin Ren<sup>1,2</sup> · Liding Chen<sup>2,3</sup>

Received: 26 June 2019 / Accepted: 24 February 2020  
© Springer Nature Switzerland AG 2020

## Abstract

The present study investigated the impacts of urban geometry on incident solar radiation on building envelopes. A three-dimensional model was developed and applied to examine these relationships, with implications for building landscapes as a potential heat source for urban heat islands. In the model, we classified building envelopes into three types, including ground, roofs, and building façades. Satisfactory model performance was confirmed by comparing measured and predicted incident solar radiation results. Furthermore, we developed the Incident Solar Radiation Prediction Index (ISRPI) to address relationships between urban geometry and incident solar radiation. Our overall results showed the solar irradiance incident on building envelopes was significantly affected by urban geometry. Building façades consistently shared a large amount of the building landscape's total surface area and therefore determined more influence on variation in incident solar radiation. Weather conditions showed strong influence on incident solar radiation, primarily due to variation in atmospheric transmittance. Diffuse radiation demonstrated a larger share of incident solar radiation on the cloudy sampling day. ISRPI, which cumulatively combined the strengths of several traditional urban morphological metrics, exhibited a strong linear relationship with incident solar radiation under sunny and cloudy weather conditions. This index provided a more convenient approach to estimate the spatial-temporal variations of solar radiations at urban scale.

**Keywords** Urban geometry · Incident solar radiation · Building envelopes · Urban heat island

## 1 Introduction

During rapid urbanization, tremendous land cover modification, and mass anthropogenic heat flux emissions remodel the energy balance of urban areas and lead to the formation of urban heat island (UHI). Many studies have revealed the plurality of environmental problems associated with UHI, including but not limited to increased energy consumption, air and water quality degradation, and negative impacts on public health [3, 10, 29, 35]. We can simply classify urban landscapes into impervious surfaces

(e.g., roads, roofs, façades) and natural landscapes (e.g., vegetation, water bodies). These surfaces are distinctly different in physical surface energy exchange processes. In contrast with natural landscapes, artificial impervious surfaces composed of asphalt and concrete are generally dark surfaces with higher thermal inertia and prone to absorb and store more solar radiation [20]. The solar absorbed by impervious surfaces is favorably partitioned into sensible heat rather than latent heat fluxes [26]. A greater percentage of impervious surfaces thus imply higher risk of degradation in urban thermal environment. Accurately calculating the percentage of impervious surfaces and the amount of incident solar radiation on these surfaces can contribute to the effective evaluation of potential heat risk.

There are multiple mitigation strategies that can be used to improve urban thermal environment. One of the most obvious approach is to revert back to the environment of the past [21]. More trees not only cool the air through evapotranspiration but also intercept solar radiation and mitigate the heating up of land surfaces [4, 37]. Other forms of greenery such as rooftop gardens and vertical greeneries have gained popularity in

✉ Zhifeng Wu  
iamwuzf@hotmail.com

<sup>1</sup> Key Laboratory of Urban Environment and Health, Fujian Key Laboratory of Watershed Ecology, Institute of Urban Environment, Chinese Academy of Sciences, Xiamen 361021, China

<sup>2</sup> University of Chinese Academy of Sciences, Beijing 100049, China

<sup>3</sup> State Key Laboratory of Urban and Regional Ecology, Research Center for Eco-Environmental Sciences, Chinese Academy of Sciences, Beijing 100085, China

recent years in fighting UHI [2]. With regard to impervious surfaces, cooling effects can be achieved by using modified pavement material such as reflective pavements, evaporative pavements, and phase change material impregnated pavements [26]. These mitigation strategies can be implemented in post-construction phase. At the pre-construction phase, the assessment of solar energy on building envelopes is essential to support the early decision making [22]. The level of solar exposure and energy performance of the built environment is strongly influenced by various factors including building morphological characteristics. Investigating the impacts of urban geometry on incident solar radiation on building envelopes helps to understand the spatial-temporal variations of solar radiations, identify the hotspots of solar potential, and apply appropriate mitigation technologies on targeted surfaces.

Accurately describing the urban landscape is vital for environmental studies and urban planning and management to gain a better understanding of the underlying mechanisms of UHI formation [6]. A considerable amount of studies has been conducted to investigate the interactions between various indicators of urban topography and land use/cover change and characteristics of urban thermal environment [9, 25, 36, 39]. One of the shortcomings in previous UHI related research is that limited emphasis has been placed on the three-dimensional features of urban area because of data and other technical problems [11]. Although several three-dimensional metrics such as sky view factor (SVF) and street canyon aspect ratio (H/W) have long been used to predict the variation of near surface air temperature, different studies have obtained contradictory results [34]. Nault et al. (2015) reviewed the performance of multiple urban morphological metrics for the solar potential and indicated that there are obvious limitations associated to using only one metric to describe the solar exposure levels and suggested upcoming work should attempt to integrate multiple simple metrics to improve the prediction performance [22].

The primary objectives of the present study were to evaluate the potential direct and diffuse solar radiation aggregated at building envelopes and analyze the impacts of canyon geometry on incident solar radiation. A numerical model derived from Geographical Information Systems (GIS) was constructed and a new geometric metrics was designed to address the following three questions: (1) how does building geometry affect surface area variation, which receives solar radiation; (2) how does building geometry influence incident solar radiation on different types of surfaces under different weather conditions; and (3) how can urban planners minimize solar radiation absorption? Our overall aim was to provide a scientific basis to accurately predict the redistribution of solar radiation under complex urban building aggregations and offer useful suggestions for urban planners and designers in the application of mitigation strategies.

## 2 Methodology

### 2.1 Location Description

Beijing is located in the northern region of the North China Plain, from 39° 28' N to 41° 04' and 115° 25' E to 117° 30' E. Beijing is characterized as a humid, continental climate with large seasonal temperature differences. The Köppen Climate Classification subtype for this climate is “Dwa,” i.e., Hot Summer Continental Climate. Beijing has experienced rapid urbanization over the last 30 years, with the urban area expanding from 801 km<sup>2</sup> in 1980 to 2452 km<sup>2</sup> in 2010 [30], and the population increasing sharply from 8.7 million in 1978 to 21.1 million in 2013 [16]. The urban thermal environment continues to suffer severe pressure from ongoing urbanization. Liu et al. (2007) compared air temperatures between Beijing’s urban and rural areas and indicated the UHI effect has progressively intensified for decades [18]. In addition, Ma et al. (2014) showed Beijing’s rapid urbanization led to increased heat wave days and simultaneously decreased precipitation during summer months [19].

To reduce the population pressure in the central districts of Beijing, several large residential areas have been constructed in suburban areas (e.g., the Tiantongyuan-Beiyuan Residential Area (TBRA)) to accommodate the growing numbers of immigrants to the city (Fig. 1a, b). On-site field measurements were conducted in a typical residential quarter (Wangchunyuan) located in TBRA from 10 to 18 August 2014 (Fig. 1c). This period was selected to obtain variable climatic data for typical summer days. An Onset HOBO® U30 weather station was positioned in an open space in a typical residential quarter. This mobile meteorological station measured a wide range of weather parameters, including shortwave solar radiation. Station data were used to verify the model results for estimating incident solar radiation. Although building configuration impacts on incident solar radiation were likely different for cities other than Beijing, the general relationship trend was expected to be similar. Thus, the results obtained here might be suitable for extrapolation to other situations.

### 2.2 Incident Solar Radiation Estimates on Building Envelopes

Urban development leads to redistribution of incident solar radiation on building envelopes. The building envelopes in the present study primarily included ground, roofs, and façade surfaces. Solar radiation loss on ground surfaces from the shading effects of surrounding buildings was compensated by the addition of solar radiation on vast roof and façade areas. The variation in losses and gains in shortwave radiation resulted in highly heterogeneous surface fluxes, which have the potential to effect local climate [24].



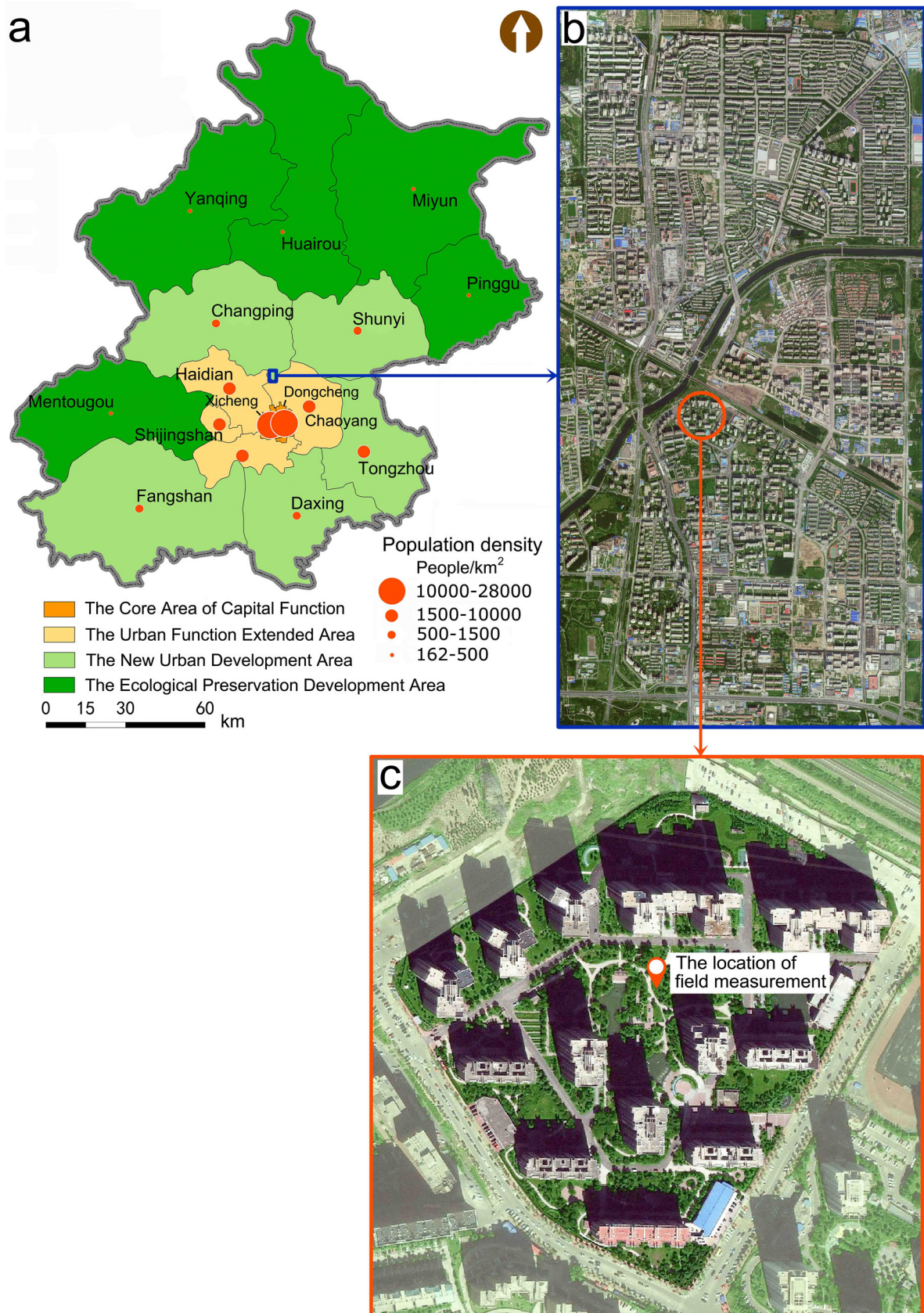


**Fig. 1** **a** The administrative map of Beijing. **b** Aerial view of the Tian tongyuan-Beiyuan Residential Area. **c** Wangchunyuan residential quarter and the location of meteorological observations

**Table 1** *P* values in different weather conditions

| Time                                     | 7:00  | 8:00  | 9:00  | 10:00 | 11:00 | 12:00 | 13:00 | 14:00 | 15:00 | 16:00 | 17:00 |
|--|-------|-------|-------|-------|-------|-------|-------|-------|-------|-------|-------|
| <i>P</i> in different weather conditions |       |       |       |       |       |       |       |       |       |       |       |
| Sunny                                    | 0.306 | 0.473 | 0.576 | 0.645 | 0.597 | 0.642 | 0.709 | 0.790 | 0.855 | 0.866 | 0.971 |
| Cloudy                                   | 0.027 | 0.026 | 0.014 | 0.031 | 0.010 | 0.049 | 0.031 | 0.051 | 0.037 | 0.871 | 0.689 |

In this study, we built a numerical model to estimate incident shortwave radiation on building envelopes. The basic algorithm to estimate solar radiation was implemented following [33]. Atmospheric transmittance is estimated using Eqs. (1) and (2). Incident shortwave radiation is the sum of direct and diffuse irradiance (3). Direct and diffuse irradiance are calculated using Eqs. (4) and (5):

$$I_{\text{standard}} = I_0 \cdot e^{-K \cdot x} \quad (1)$$

$$P = I_{\text{measured}} / I_{\text{standard}} \quad (2)$$

$$I_{\text{estimated\_sum}} = I_{\text{estimated\_direct}} + I_{\text{estimated\_diffuse}} \quad (3)$$

$$I_{\text{estimated\_direct}} = I_0 \cdot P^{1/\sinh} \cdot \cos\theta \quad (4)$$

$$I_{\text{estimated\_diffuse}} = -0.5 \cdot I_0 \cdot \sinh \cdot \frac{1 - P^{1/\sinh}}{1 - 1.4 \ln P} \quad (5)$$

where  $I_0$  is the solar constant with a value of  $1367 \text{ W/m}^2$ ;  $K$  is the extinction coefficient, referring to the light absorption measure through atmosphere by water vapor and aerosol;  $x$  is distance through the atmosphere, which is calculated applying solar altitude ( $h$ ) and solar incidence angle ( $\theta$ );  $I_{\text{standard}}$  is solar radiation striking earth's surface under the assumption of a completely transparent atmosphere ( $K = 1$ );  $P$  is atmospheric transmittance estimated by comparing measured and predicted solar radiance (Table 1); and  $I_{\text{estimated\_sum}}$ ,  $I_{\text{estimated\_direct}}$ , and  $I_{\text{estimated\_diffuse}}$  are estimated total solar radiation, estimated direct

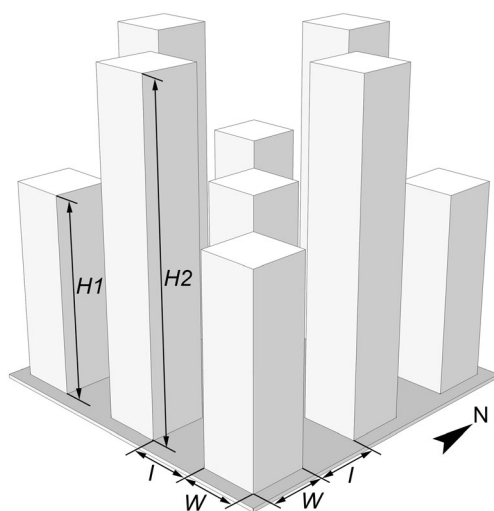
solar radiation, and estimated diffuse radiation reaching ground surfaces, respectively.

Different building configuration scenarios were built on the ArcGIS® platform. All surfaces, including the ground, the façades, and the roofs, were divided into regular square grids. Each element of the grid corresponds to an area of  $1 \times 1 \text{ m}$ . Python was used to automate the calculation of incident solar radiation on surfaces every 10 min during the selected daytime period on ArcGIS® platform. Direct and diffuse solar radiation reached at each surface type was calculated. The study conducted by Yan and Zhao (1986) indicated low solar altitude effected the accuracy of results [33]; therefore, we selected the time interval from 7:00 to 18:00 in summer to calculate incident solar radiation. Using this model, we obtained active surface areas receiving direct solar radiation, direct and diffuse solar radiation cast on each surface type, and variation in incident solar radiation.

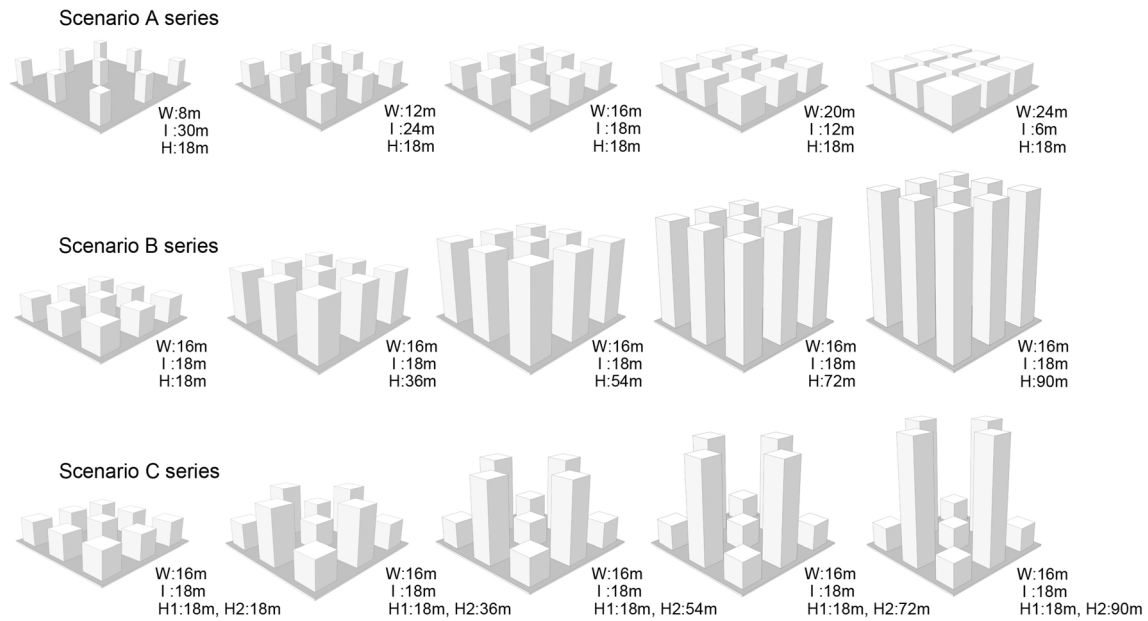
### 2.3 Different Urban Geometry Scenarios

Figure 2 presents the main morphometric parameters, including building height ( $H$ ), building interval ( $I$ ), and building width/length ( $W$ ) used to define the urban geometry scenarios. Nine buildings were evenly distributed on a square land parcel ( $84 \times 84 \text{ m}$ ) (Fig. 2).

The influence of urban geometry on incident solar radiation was evaluated in three different scenarios. The A and B scenarios were designed to examine building impacts on incident solar radiation in terms of area building density and height variability (Fig. 3). Both scenario series exhibited increased floor area ratio (FAR), decreased SVF, and varied surface area receiving solar radiation. The following parameters were established for each scenario (A, B, and C): Scenario A varied building width/length and building interval, while building height remained constant; scenario B maintained building width/length and intervals remained unchanged (16 m and 18 m), respectively, while building height increased linearly from 18 m to 90 m; scenario C fixed building width/length and building interval, but integrated two building heights to study the effects of height irregularities on lower building roof solar densities. In addition, FAR and SVF were calculated for each scenario to indicate the variation of urban morphology (Table 2). FAR was calculated using Eq. (6). SVF is a parameter frequently used in urban thermal environment studies. It measures the degree the sky is observed from a given point. This parameter is a dimensionless index with scores ranging

**Fig. 2** Description of urban geometry parameters





**Fig. 3** Urban geometry of the study scenarios (W, building width/length; L, building interval; H, building height)

from 0 to 1, where 0 represents absolutely no sky seen from the target point and 1 represents a complete view of the sky [17]. We calculated SVF using Rayman, developed by the Meteorological Institute, University of Freiburg [13]. We calculated not only the SVF of the ground area of the square land parcel that has not been occupied by buildings but also the ground area surrounding the land parcel in consideration of the shading effect of buildings on this region. An 84-m-deep border was added to the perimeter of the square land parcel, and the whole landscape structure was used to calculate SVF using Rayman.

$$FAR = \frac{\sum_{i=1}^n (\text{Number}_f \times \text{Area}_f)}{\text{Area}_p} \quad (6)$$

**Table 2** The values of FAR and SVF for each scenario series

| Name                   | Value       |       |       |       |       |
|------------------------|-------------|-------|-------|-------|-------|
| Floor area ratio (FAR) | Scenario A1 | A2    | A3    | A4    | A5    |
|                        | 0.49        | 1.10  | 1.96  | 3.06  | 4.41  |
|                        | Scenario B1 | B2    | B3    | B4    | B5    |
|                        | 1.96        | 3.92  | 5.88  | 7.84  | 9.80  |
|                        | Scenario C1 | C2    | C3    | C4    | C5    |
| Sky view factor (SVF)  | 1.96        | 2.83  | 3.70  | 4.57  | 5.44  |
|                        | Scenario A1 | A2    | A3    | A4    | A5    |
|                        | 0.845       | 0.738 | 0.606 | 0.442 | 0.24  |
|                        | Scenario B1 | B2    | B3    | B4    | B5    |
|                        | 0.606       | 0.497 | 0.466 | 0.453 | 0.447 |
| Scenario C1            | C2          | C3    | C4    | C5    |       |
|                        | 0.606       | 0.54  | 0.509 | 0.492 | 0.481 |

where  $\text{Number}_f$  is the number of floors.  $\text{Area}_f$  is the floor area, and  $\text{Area}_p$  is the land parcel area ( $84 \times 84$  m).

Two weather conditions (sunny and cloudy) with different  $P$  values (Table 1) were selected to represent the influence of water vapor or atmospheric particulates on incident solar radiation.

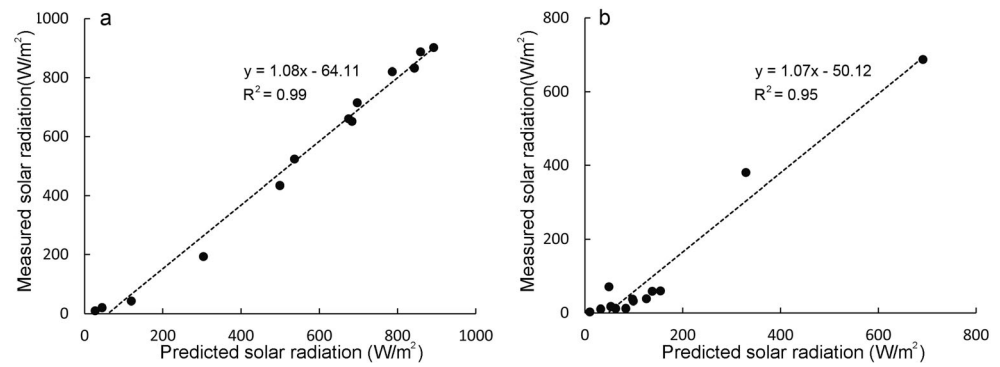
## 2.4 Derivation of Incident Solar Radiation Prediction Index

In addition to the abovementioned two urban morphological metrics, a new metric (Incident Solar Radiation Prediction Index—ISRPI) was constructed to describe the incident solar radiation levels casted on all types of building landscape surfaces with different urban geometry. The definition of the new parameter (ISRPI) took three important factors (surface area, building height, and SVF) into consideration. SVF, which represents the proportion of the sky that is visible from a target point, has been used for estimating the solar energy potential in urban environments in previous study [8]. ISRPI is a non-dimensional parameter. With the value of ISRPI increases from zero, the urban geometry will transform from low-rise and high-density type to high-rise and low-density type. ISRPI was calculated using Eq. (7).

$$ISRPI = \left( \frac{\text{Area}_t}{\text{Area}_p} \right) \cdot \left( \frac{\text{Height}_{\text{ave}}}{\text{Height}_{\text{max}}} \right) \cdot \text{SVF} \quad (7)$$

where  $\text{Area}_p$  represents the land parcel area where nine buildings were evenly distributed ( $84 \times 84$  m) and  $\text{Area}_t$  is the total surface area of all buildings.  $\text{Height}_{\text{ave}}$  is the average height of all nine buildings and  $\text{Height}_{\text{max}}$  is the maximum building height on the ground parcel ( $\text{Height}_{\text{max}}=90$  m in this study).

**Fig. 4** The relationship between measured and predicted solar radiation at ground surface. **a** Sunny day. **b** Cloudy day



### 3 Results

#### 3.1 Model Validation

Model verification was conducted based on field measurement data. We chose one sunny and one cloudy day (10 and 14 August 2014, respectively) to estimate incident shortwave irradiance at ground surface. We compared measured and predicted shortwave solar irradiance at ground surface from 7:00 to 18:00. On the sunny day, the model performed better during 10:00 to 17:00, with the residual error ratio ( $\frac{I_{\text{predicted}} - I_{\text{measured}}}{I_{\text{measured}}} \times 100\%$ ) varying between 1.1% (15:00) and 4.6% (16:00), than the hours before 10:00 and after 17:00, particularly between 6:00 and 8:00 a.m. The average difference between measured and predicted results was 21.1 W/m<sup>2</sup>. Figure 4 shows the relationship between measured and predicted solar radiation with a high  $R^2$ -value for the sunny day ( $R^2 = 0.99$ ). On the cloudy day, however, the residual error ratio increased for the entire day, but it remained a strong

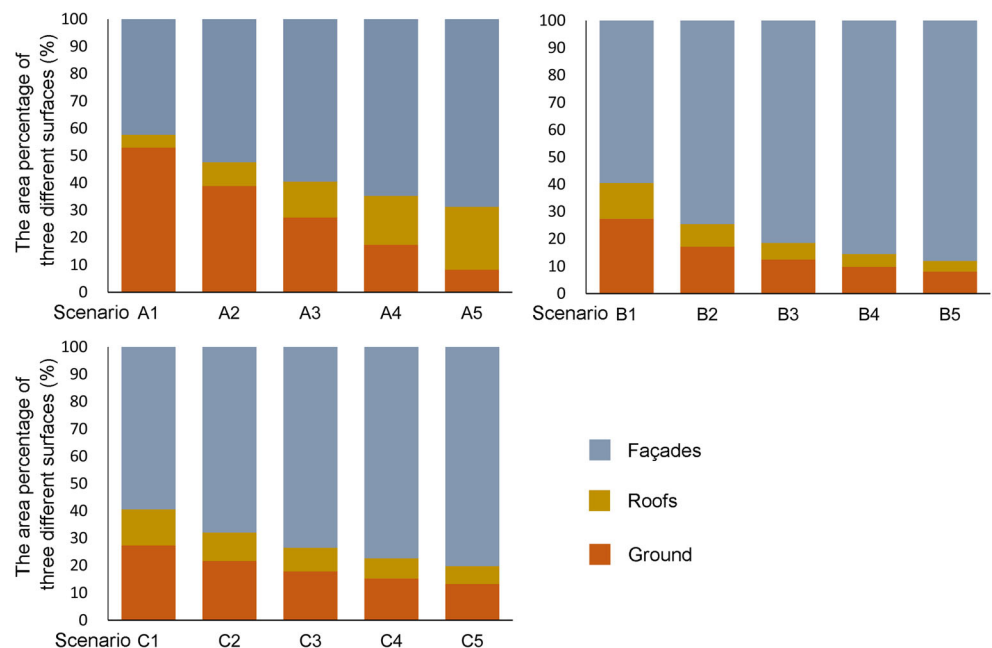
relationship ( $R^2 = 0.95$ ) between measured and predicted values. These results indicated the empirical model met the research requirements for estimating incident shortwave irradiance.

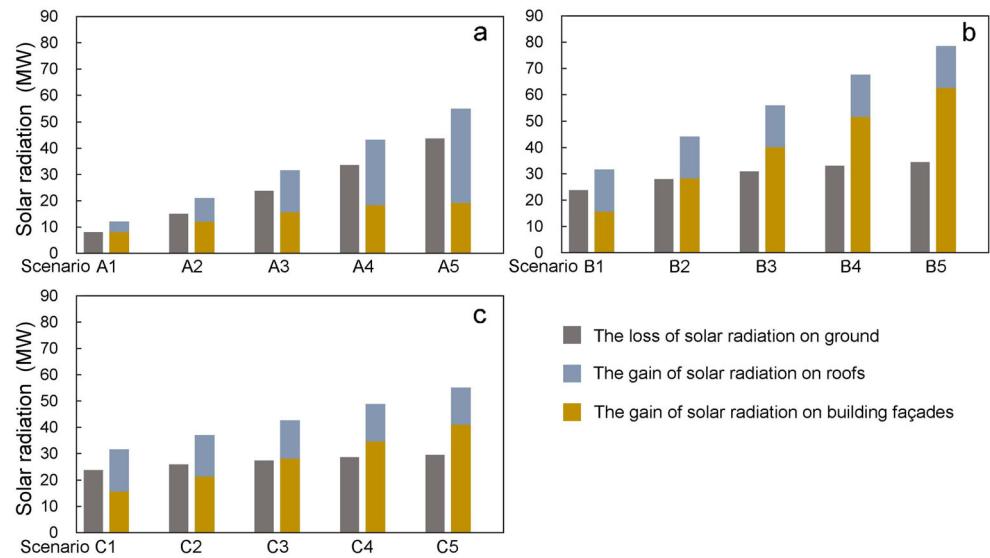
#### 3.2 Variation in Surface Area and Incident Solar Radiation

We here present the variation in surface area and the amount of incident solar radiation in post-construction phase, in contrast with the undeveloped state of the land parcel without any building on it.

The total surface areas (Area<sub>t</sub>) included ground surfaces not occupied by buildings and roof and façade areas, which ranged from 12,240 to 22,608 m<sup>2</sup> for scenario A, 17,424 m<sup>2</sup> to 58,896 m<sup>2</sup> for scenario B, and 17,424 m<sup>2</sup> to 35,856 m<sup>2</sup> for scenario C. Compared with the square land parcel area ( $84 \times 84 \text{ m} = 7056 \text{ m}^2$ ) where buildings were distributed, results indicated the increase in surface areas that can receive solar

**Fig. 5** Area percentage of the three different surfaces

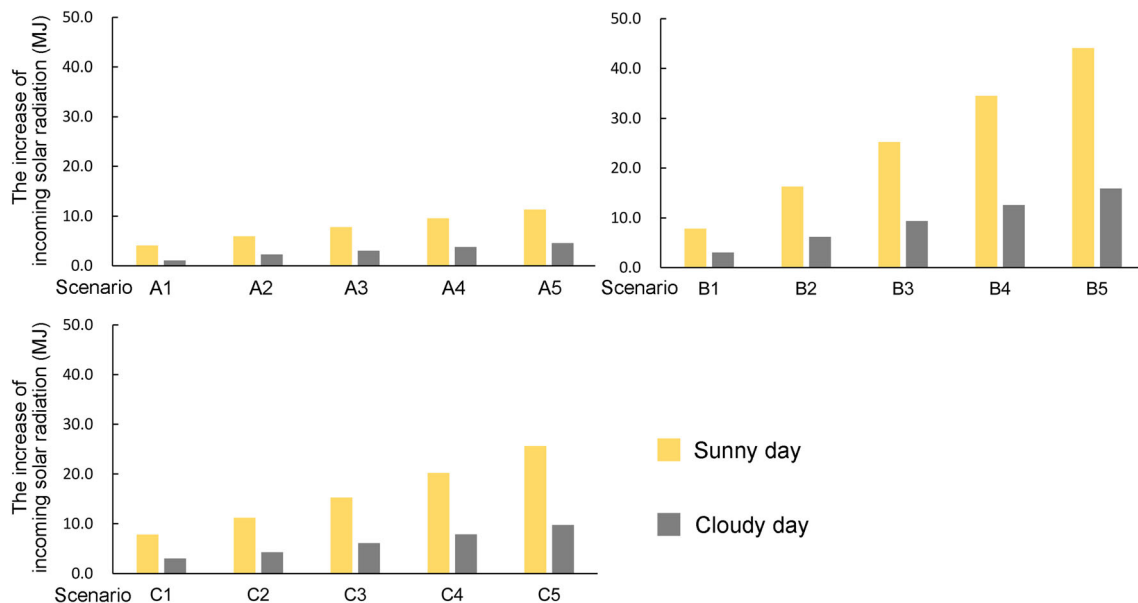


**Fig. 6** Incident solar radiation variation under different urban geometric scenarios

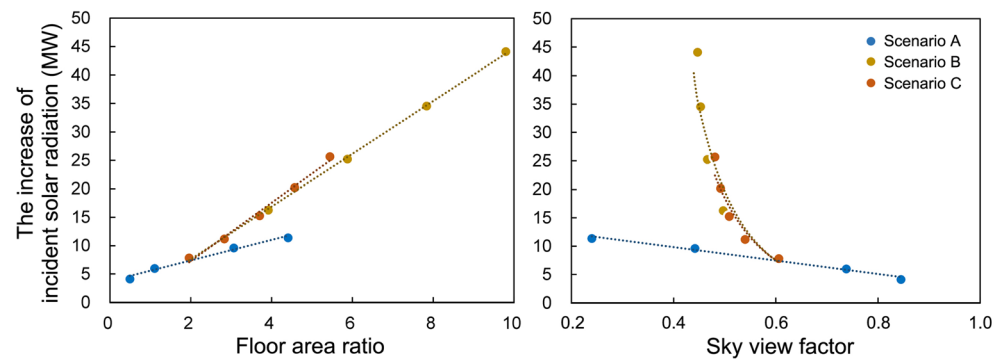
radiation was at least 73.4% (scenario A1), with a maximum of 734.7% (scenario B5). Among the three types of surfaces, façades consistently showed a large amount of the total surface area (Fig. 5) and with the increase of FAR, the façades' area increased markedly. For example, the façade area for scenario B5 reached as much as 88.02% of total surface area. The variation in roof and ground surface areas, however, showed different trends. For scenario A series (from A1 to A5), results revealed with increased FAR, roof area also increased gradually, however ground surface decreased accordingly. Scenarios B and C series showed a downward trend in roof and ground surfaces.

Building construction leads to the redistribution of incident solar radiation. Some ground surfaces could no longer receive solar radiation due to building coverage. Ground surfaces lost

direct solar radiation by shading of surrounding buildings. Other two surface types increased the potential reception of incident solar radiation. Figure 6 represents the loss and increase of incident solar radiation under different scenarios developed in this study. For all three scenarios, the increase exceeds the loss of solar radiation. Scenario A shows a gradually increasing trend for both loss and gain of solar radiation from scenario A1 to scenario A5. There were 4.11 MW (A1), 5.97 MW (A2), 7.82 MW (A3), 9.60 MW (A4), and 11.37 MW (A5) more incident solar radiation comparing with pre-construction phase. The loss of solar radiation in scenario B series maintained almost unchanged, while the amount of incident solar radiation on building façades and roofs showed notably increase. Building façades accounted for a much larger portion of the gain of solar radiation. There were 7.82 MW,

**Fig. 7** Incident solar radiation variation under two different weather conditions

**Fig. 8** Incident solar radiation variation for different floor area ratio and sky view factor (SVF)



16.27 MW, 25.22 MW, 34.53 MW, and 44.10 MW more incident solar radiation respectively for scenario B series. Similarly, there were obvious increase of incident solar radiation in scenario C series.

### 3.3 Incident Solar Radiation Variation Under Different Weather Conditions

We calculated incident solar radiation casted on all surfaces using three geometric scenarios under two weather conditions, i.e., sunny and cloudy days (Table 1). The total incident solar radiation, including direct and diffuse irradiance measured from 7:00 to 18:00, was summed as one value for each scenario. For three scenario series, the incident solar radiation values under the sunny day were 2.81 (scenario A), 2.68 (scenario B), and 2.57 (scenario C) times the amount of irradiance reaching surfaces under the cloudy day. Scenario A series's solar radiation ratio between sunny and cloudy days showed a tendency to decrease with FAR increase. For scenario B and C series, however, the ratio represented a gradually increased trend from scenario B1 (C1) to scenario B5 (C5) (Fig. 7).

### 3.4 Relationship Between Incident Solar Radiation with Traditional and Newly Developed Indices

We analyzed the relationships between incident solar radiation and two commonly used indices that represent building density (Fig. 8). The results showed incident solar radiation casted on total surfaces of all three geometric scenario series

increased linearly with FAR. Scenarios B and C represented similar increases, followed by scenario A, where results demonstrated a lower increased rate. When the FAR was 4, for example, the incident solar radiation for three geometric scenarios were 17.56 MW, 16.87 MW, and 11.02 MW, respectively. The relationship between incident solar radiation and SVF, however, is not that explicit. For scenario A, incident solar radiation decreased with increased SVF. Scenarios B and C showed a non-linear relationship with SVF.

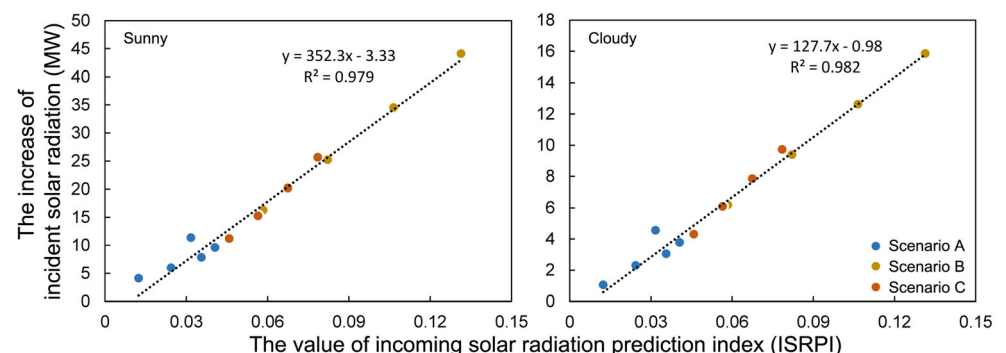
However, incident solar radiation exhibited a strong linear relationship with ISRPI, regardless of sunny ( $R^2 = 0.979$ ) or cloudy ( $R^2 = 0.982$ ) days, which indicated the index was a reliable predictor of incident solar radiation (Fig. 9).

## 4 Discussion

### 4.1 Implications for Urban Planning

Researchers and urban planners have widely viewed greenspaces as one of the most effective strategies to counteract the effects of urban warming trends [1, 23]. Many greenspace types, including urban forests, parks, roadside trees, private and public gardens, and vegetated roofs/facades, are applied to circumvent the massive transformation of natural surfaces to impervious alternatives [2, 7]. By rational selection of plant species and optimizing greenspace locations, researches demonstrated the cooling effects of vegetation on specific areas were improved [31, 38]. However, it

**Fig. 9** Incident solar radiation variation for different ISRPI





should be noted most greenspace rearrangements are based on certain impervious surface landscape patterns. Therefore, the contributions of the impervious surface landscape pattern to UHI altitude influences the potential cooling power of specific greenspaces [27]. Under these circumstances, researchers and urban planners should consider the impacts of artificial structures on urban thermal environments from a project's onset. Optimizing impervious surface patterns, especially building patterns, is a promising strategy from the perspective of mitigating UHI effects [15, 28, 32]. In the present study, we investigated incident solar radiation impacts based on building patterns by constructing three building geometric scenarios representing two distinct urban development modes. Scenario A, which has lower building height and varying building intervals, is still common in suburban and some urban areas. Scenarios B and C are becoming mainstream in commercial and residential development, especially in central urban areas. Our results showed three scenarios have different growth rates of incident solar radiation, with increased FAR. Scenario A showed lower incident solar radiation for the FAR from 1.96 to 4.41 compared with scenarios B and C; therefore, this geometric scenario likely absorbed less solar radiation and contributed reduced sensible heat flux into the surrounding atmosphere. However, the increased FAR revealed for scenario A was due to the reduced interval between neighboring buildings, consequently it can only change within a certain range under fixed building height. It might be necessary for urban planners to make a tradeoff between scenario A and scenarios B and C to accommodate continuous population growth in urban areas and to improve the urban thermal environment, the current target. Roofs and building façades played different roles in the gain of solar radiation in different scenarios. In scenario A, the roofs had greater potential in receiving incident solar radiation comparing with building façades. For scenario B and scenario C, however, building façades contributed more to the variation of total incident solar radiation. It can help us to determine the priority in implementing horizontal or vertical greening systems for improving local thermal environment.

Solar radiation is the driving force of surface thermal flux processes and surface temperature depends primarily on incident solar radiation levels [34]. Thermal characteristics of urban landscapes might efficiently be described by accurate estimates of incident solar radiation. Previous studies related to solar availability on urban surfaces and surface temperatures employed numerous variables to describe variation in urban geometry. Chatzipoulka et al. (2016) analyzed the relationships among ten variables, including site area coverage, mean building height, building compactness, and solar availability on ground and façades [9]. Their results showed diverse building arrangements significantly effected incident solar radiation, which was influenced by different variables for specific surfaces (ground and façades), and seasons (winter and

summer). Guo et al. (2016) used variables to describe variation in ground surface temperatures derived from infrared remote sensing images, including building height and density and SVF [14]. Previous research presented complex relationships between urban geometry and solar availability or surface temperature and therefore it remains inaccurate to use one single index or linear equation to describe this relationship. Non-linear relationships are often tricky in prediction due to uneven rates of change. In the present study, we developed a new index, which integrates building density and height heterogeneity to characterize the variation in incident solar radiation reaching urban surfaces. Our index provides a more convenient approach to estimate the spatial distribution of incident solar radiation, and helps to identify the hotspots of solar potential at urban scale. Furthermore, this index might help to improve accuracy of forecast and early warning against thermal stress in summer season.

We also examined the incident solar radiation of three scenarios under two different weather conditions. Results showed the incident solar radiation under the sunny sample day was roughly 2.6 times the amount from the cloudy sample day. The much larger atmospheric transmittance difference between two weather conditions (Table 1) indicated diffuse irradiance is an important solar resource variable [5] and should not be excluded when improving urban thermal comfort levels, i.e., not just direct irradiance.

## 4.2 Advantages and Limitations

Our study employed GIS based on ArcGIS® to investigate how urban geometry influenced incident solar radiation casted on all surfaces, including ground surfaces, roofs, and façades. The technique exhibited some advantages compared with other methods used for this purpose. First, our method was based on vector models, which are more straightforward and accurate in describing building outlines than those based on raster models. Second, the methods based on common GIS platforms bridge the gap between urban climatology research and urban planning processes. Building volumes are recognized as polygons, where building heights are stored in attribute tables. This method avoids, to a large extent, complicated modeling and mathematics. However, several limitations remain, which should be improved in future study. First, pursuit of a simple and practical modeling method resulted in the sacrifice of some complicated processes, such as multi-reflection among surfaces, but the method maintained relatively high accuracy (Fig. 3). Second, we only conducted the research in one city and the model was developed to assess incident solar radiation differently on urban surfaces with variation in solar altitude. However, our model and ISRPI were feasible to apply because it only required building landscape data in a city.

This study was conducted in Beijing, which is located at the northern hemisphere. All direct solar radiation was casted on east, south, and west wall. There was nearly no direct solar radiation can be received by the north wall even on the summer solstice. There is significant difference of incoming solar radiation on urban surfaces of cities locate on different latitudes. Further studies should be carried out to verify ISRPI's availability on other cities. Another limitation of this study is the absence of vegetation. The distribution and coverage of vegetation can significantly affect the calculation of solar potentials on urban surfaces. Researchers have developed a method to calculate solar-related indicators (e.g., SVF) based on detailed building and vegetation database [12]. The database was obtained using digital photogrammetric methods for tree height measurement and spectral information from aerial photograph. The influence of vegetation, especially trees, on solar potentials on urban surfaces will be considered in future studies of ISRPI.

## 5 Conclusions

A three-dimensional model for incident solar radiation casted on urban surfaces, including ground, roofs, and façade surfaces, was developed and applied to assess the potential impact of urban geometry on UHI effects. The results showed the following: (1) urban geometry exhibited notable influence on variation in building landscape surface area; a marked share of the total surface area was consistently occupied by façades and therefore this surface showed a high contribution to receiving incident solar radiation; (2) incident solar radiation was markedly decreased under the cloudy sample day in contrast with the sunny sample day; however, the difference between incident solar radiations was smaller than the difference in atmospheric transmittances between the two weather conditions, which indicated the diffuse solar radiation occupied an important position in total incident solar radiation; and (3) results demonstrated the newly developed index, ISRPI, which comprehensively combined FAR, building height heterogeneity, and SVF, was more accurate in predicting incident solar radiation for specific building landscapes. Furthermore, some suggestions have been proposed in view of existing problems of urban form optimization and urban greening.

**Acknowledgments** We are grateful to the anonymous reviewers for their constructive suggestions.

**Funding Information** This work was supported by the National Science Foundation of China (41801182, 31670645, 31972951, 31470578, 31200363, 41590841, and 41807502), National Social Science Foundation of China (17ZDA058), and the National Key Research Program of China (2016YFC0502704).

## References

1. Akbari, H., Davis, S., Dorsano, S., Huang, J. and Winnett, S. (1992). *Cooling Our Communities: A Guidebook on Tree Planting Light-Colored Surfacing*. U.S. Environmental Protection Agency, Office of Policy Analysis, Climate Change Division.
2. Akbari, H., & Kolokotsa, D. (2016). Three decades of urban heat islands and mitigation technologies research. *Energy and Buildings*, 133, 834–842.
3. Amberger, A., Alex, B., Eder, R., Ebenberger, M., Wanka, A., Kolland, F., Wallner, P., & Hutter, H.-P. (2017). Elderly resident's uses of and preferences for urban green spaces during heat periods. *Urban Forestry & Urban Greening*, 21, 102–115.
4. Balogun, A. A., Morakinyo, T. E., & Adegun, O. B. (2014). Effect of tree-shading on energy demand of two similar buildings. *Energy and Buildings*, 81, 305–315.
5. Battles, F. J., Olmo, F. J., & Alados-Arboledas, L. (1995). On shadowband correction methods for diffuse irradiance measurements. *Solar Energy*, 54(2), 105–114.
6. Berger, C., Rosentreter, J., Voltersen, M., Baumgart, C., Schmulilius, C., & Hese, S. (2017). Spatio-temporal analysis of the relationship between 2D/3D urban site characteristics and land surface temperature. *Remote Sensing of Environment*, 193(Supplement C), 225–243.
7. Bowler, D. E., Buyung-Ali, L., Knight, T. M., & Pullin, A. S. (2010). Urban greening to cool towns and cities: a systematic review of the empirical evidence. *Landscape and Urban Planning*, 97, 147–155.
8. Calcabrini, A., Ziar, H., Isabella, O., & Zeman, M. (2019). A simplified skyline-based method for estimating the annual solar energy potential in urban environments. *Nature Energy*, 4(3), 206–215.
9. Chatzipoulka, C., Compagnon, R., & Nikolopoulou, M. (2016). Urban geometry and solar availability on façades and ground of real urban forms: using London as a case study. *Solar Energy*, 138, 53–66.
10. Chen, Y., Wang, X., Jiang, B., Wen, Z., Yang, N., & Li, L. (2017). Tree survival and growth are impacted by increased surface temperature on paved land. *Landscape and Urban Planning*, 162, 68–79.
11. Chun, B., & Guldman, J.-M. (2014). Spatial statistical analysis and simulation of the urban heat island in high-density central cities. *Landscape and Urban Planning*, 125, 76–88.
12. Gál, T., & Unger, J. (2014). A new software tool for SVF calculations using building and tree-crown databases. *Urban Climate*, 10(Part 3), 594–606.
13. Gulyás, Á., Unger, J., & Matzarakis, A. (2006). Assessment of the microclimatic and human comfort conditions in a complex urban environment: modelling and measurements. *Building and Environment*, 41(12), 1713–1722.
14. Guo, G., Zhou, X., Wu, Z., Xiao, R., & Chen, Y. (2016). Characterizing the impact of urban morphology heterogeneity on land surface temperature in Guangzhou, China. *Environmental Modelling and Software*, 84, 427–439.
15. Hsieh, C.-M., Chen, H., Ooka, R., Yoon, J., Kato, S., & Miisho, K. (2010). Simulation analysis of site design and layout planning to mitigate thermal environment of riverside residential development. *Building Simulation*, 3(1), 51–61.
16. Jia, Q. (2014). *Beijing statistics yearbook*. Beijing: China Statistical Press.
17. Lindberg, F., & Grimmond, C. S. B. (2010). Continuous sky view factor maps from high resolution urban digital elevation models. *Climate Research*, 42(3), 177–183.
18. Liu, W., Ji, C., Zhong, J., Jiang, X., & Zheng, Z. (2007). Temporal characteristics of the Beijing urban heat island. *Theoretical and Applied Climatology*, 87(1), 213–221.

19. Ma, H., Shao, H., & Song, J. (2014). Modeling the relative roles of the foehn wind and urban expansion in the 2002 Beijing heat wave and possible mitigation by high reflective roofs. *Meteorology and Atmospheric Physics*, 123(3–4), 105–114.
20. Memon, R. A., Leung, D. Y. C., & Chunho, L. (2008). A review on the generation, determination and mitigation of urban heat island. *Journal of Environmental Sciences*, 20, 120–128.
21. Mohajerani, A., Bakaric, J., & Jeffrey-Bailey, T. (2017). The urban heat island effect, its causes, and mitigation, with reference to the thermal properties of asphalt concrete. *Journal of Environmental Management*, 197(Supplement C), 522–538.
22. Nault, E., Peronato, G., Rey, E., & Andersen, M. (2015). Review and critical analysis of early-design phase evaluation metrics for the solar potential of neighborhood designs. *Building and Environment*, 92, 679–691.
23. Oke, T. R. (1979). Advectively-assisted evapotranspiration from irrigated urban vegetation. *Boundary-Layer Meteorology*, 17(2), 167–173.
24. Oke, T. R. (1987). *The boundary layer climates* (2nd ed.). London and New York: Methuen.
25. Peng, J., Xie, P., Liu, Y., & Ma, J. (2016). Urban thermal environment dynamics and associated landscape pattern factors: a case study in the Beijing metropolitan region. *Remote Sensing of Environment*, 173, 145–155.
26. Qin, Y. (2015). A review on the development of cool pavements to mitigate urban heat island effect. *Renewable and Sustainable Energy Reviews*, 52, 445–459.
27. Tan, Z., Lau, K. K.-L., Ng, E. (2016). Urban tree design approaches for mitigating daytime urban heat island effects in a high-density urban environment. *Energy and Buildings*, 114, 265–274.
28. Wang, Y., Berardi, U., Akbari, H. (2016). Comparing the effects of urban heat island mitigation strategies for Toronto, Canada. *Energy and Buildings*, 114, 2–19.
29. Ward, K., Lauf, S., Kleinschmit, B., & Endlicher, W. (2016). Heat waves and urban heat islands in Europe: a review of relevant drivers. *Science of the Total Environment*, 569–570, 527–539.
30. Wu, W., Zhao, S., Zhu, C., & Jiang, J. (2015). A comparative study of urban expansion in Beijing, Tianjin and Shijiazhuang over the past three decades. *Landscape and Urban Planning*, 134, 93–106.
31. Wu, Z., & Chen, L. (2017). Optimizing the spatial arrangement of trees in residential neighborhoods for better cooling effects: integrating modeling with in-situ measurements. *Landscape and Urban Planning*, 167, 463–472.
32. Xuan, Y., Yang, G., Li, Q., & Mochida, A. (2016). Outdoor thermal environment for different urban forms under summer conditions. *Building Simulation*, 9(3), 281–296.
33. Yan, Q., & Zhao, Q. (1986). *Heat process of building*. Beijing: Building Industry Press of China.
34. Yang, X., & Li, Y. (2015). The impact of building density and building height heterogeneity on average urban albedo and street surface temperature. *Building and Environment*, 90, 146–156.
35. Yoshikado, H., & Tsuchida, M. (1995). High levels of winter air pollution under the influence of the urban heat island along the shore of Tokyo Bay. *Journal of Applied Meteorology*, 35(10), 1804–1814.
36. Yuan, F., & Bauer, M. E. (2007). Comparison of impervious surface area and normalized difference vegetation index as indicators of surface urban heat island effects in Landsat imagery. *Remote Sensing of Environment*, 106(3), 375–386.
37. Zhang, B., Xie, G.-D., Gao, J.-X., & Yang, Y. (2014). The cooling effect of urban green spaces as a contribution to energy-saving and emission-reduction: a case study in Beijing, China. *Building and Environment*, 76, 37–43.
38. Zhao, Q., Wentz, E. A., & Murray, A. T. (2017). Tree shade coverage optimization in an urban residential environment. *Building and Environment*, 115, 269–280.
39. Zhou, W., Wang, J., & Cadenasso, M. L. (2017). Effects of the spatial configuration of trees on urban heat mitigation: a comparative study. *Remote Sensing of Environment*, 195, 1–12.

**Publisher's Note** Springer Nature remains neutral with regard to jurisdictional claims in published maps and institutional affiliations.